PHYSICAL REVIEW B **99**, 041101(R) (2019)

Rapid Communications

Band crossings in honeycomb-layered transition metal compounds

Yusuke Sugita and Yukitoshi Motome
Department of Applied Physics, The University of Tokyo, Bunkyo, Tokyo 113-8656, Japan

(Received 12 May 2018; published 2 January 2019)

Two-dimensional electron dispersions with peculiar band crossings provide a platform for realizing topological phases of matter. Here, we theoretically show that the e_g-orbital manifold of honeycomb-layered transition metal compounds accommodates a plethora of peculiar band crossings, such as multiple Dirac point nodes, semi-Dirac point nodes, quadratic band crossings, and line nodes. From a tight-binding analysis, we find that the band topology is systematically changed by the orbital-dependent transfer integrals on the honeycomb network of edge-sharing octahedra, which can be modulated by distortions of the octahedra as well as chemical substitutions. The band crossings are gapped out by spin-orbit coupling, which brings about a variety of topological phases distinguished by the spin Chern numbers. The results provide a comprehensive understanding of the previous studies on various honeycomb compounds. We also propose another candidate materials by *ab initio* calculations.

DOI: 10.1103/PhysRevB.99.041101

Two-dimensional materials with a layered structure have attracted considerable attention as a good playground for topological states of matter. The representative example is monolayer graphene composed of a purely two-dimensional honeycomb network of carbon atoms [1]. The low-energy excitation in graphene is governed by π electrons in $2p$ orbitals, whose energy dispersion has linear band crossings with the Dirac point nodes (DPNs) at the Fermi level, called Dirac cones. Stimulated by a theoretical proposal that the Dirac electron system is potentially changed into a $\mathbb{Z}_2$ topological insulator by relativistic spin-orbit coupling (SOC) [2,3], graphene and similar honeycomb-monolayer forms of Si and Ge have been studied [4,5]. In addition, few-layer graphene has also received attention as the low-energy spectrum takes a peculiar form depending on the stacking manner. For instance, in a bilayer system with so-called AB stacking, DPNs turn into quadratic band crossings (QBCs). As the QBCs possess an instability toward a quantum anomalous (spin) Hall state [6,7], the effect of electron correlations has been intensively studied in bilayer graphene [8–11].

Recently, transition metal (TM) compounds with a similar honeycomb-layered structure have gained great interest from the peculiar band topology in their d-orbital manifolds. For instance, DPNs, QBCs, and topological phases were found in systems with a corner-sharing network of octahedral ligands, e.g., [111] layers of the perovskite structure [12–16], and with edge-sharing octahedra, e.g., trichalcogenides [17], trihalides [18–21], corundum [22,23], and rhombohedral materials [24–26]. Interestingly, the number and position of the DPNs as well as the shape of the Dirac dispersions strongly depend on the materials. This indicates that the honeycomb-layered TM compounds potentially provide a variety of the band crossings and topological phases with controllability by the d-orbital degrees of freedom.

In this Rapid Communication, we theoretically show that e_g-orbital systems with edge-sharing octahedra can host a plethora of peculiar band crossings and associated topological phases of matter. Analyzing a tight-binding model for the e_g manifold, we find that a variety of band crossings appears at half filling of the e_g electrons, such as multiple DPNs, semi-DPNs, QBCs, and line nodes. We find that the band topology changes systematically for orbital-dependent transfer integrals, which can be controlled by distortions of the ligand octahedra as well as chemical substitutions. We also show that the SOC turns the electronic states with the different band crossings into different types of topological phases characterized by spin Chern numbers, some of which are unusually high or $\mathbb{Z}_2$ nontrivial. Our results provide a systematic understanding of the existing *ab initio* studies for honeycomb-layered TM compounds. Furthermore, we propose candidate materials by using *ab initio* calculations, which potentially realize a wide variety of peculiar band topologies.

We consider a tight-binding model for the e_g-orbital electrons on a honeycomb network of edge-sharing octahedra as shown in Fig. 1(a). In this structure, the important contributions to the transfer integrals come from the indirect paths via the ligand p orbitals, as the wave functions of the e_g orbitals have large amplitudes in the ligand directions. We take into account the two types of dominant transfer integrals between the same e_g orbitals for nearest and third neighbors, t_1 and t_3, as shown by the magenta and cyan lines in Fig. 1(a), respectively, and construct a tight-binding Hamiltonian compatible with the trigonal symmetry of the honeycomb lattice. The Hamiltonian is given as

$$H = t_1 \sum_{\langle ij\rangle mn\sigma} (\hat{\gamma}_{\alpha_{ij}})_{mn} c^{\dagger}_{im\sigma} c_{jn\sigma} + t_3 \sum_{\langle ij\rangle' mn\sigma} (\hat{\gamma}_{\alpha_{ij}})_{mn} c^{\dagger}_{im\sigma} c_{jn\sigma}, \tag{1}$$

where $c^{\dagger}_{im\sigma}$ ($c_{im\sigma}$) is the creation (annihilation) operator of an electron for site i, orbital $m = d_{3z^2-r^2}$ or $d_{x^2-y^2}$, spin $\sigma = \uparrow$ or $\downarrow$; $\langle ij\rangle$ ($\langle ij\rangle'$) denotes the nearest (third) neighbors, and $\alpha_{ij} =$ 1, 2, or 3 denotes the bond direction between the sites i and j in Fig. 1(a). The matrices $\hat{\gamma}_{\alpha_{ij}}$ are obtained as $\hat{\gamma}_1 = \left(\begin{smallmatrix} 0 & 0 \\ 0 & 1 \end{smallmatrix}\right)$, $\hat{\gamma}_2 = \hat{\Theta}\hat{\gamma}_1\hat{\Theta}^{-1}$, and $\hat{\gamma}_3 = \hat{\Theta}\hat{\gamma}_2\hat{\Theta}^{-1}$, where $\hat{\Theta}$ is the threefold

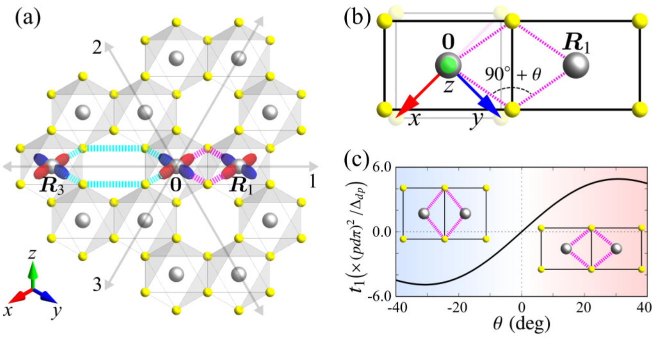

FIG. 1. (a) Schematic picture of a monolayer of honeycomb-layered TM compounds. The gray and yellow spheres represent the TM cations and the ligand ions, respectively. The magenta and cyan dotted lines denote indirect paths of nearest- and third-neighbor transfers t_1 and t_3, respectively, between the $d_{x^2-y^2}$ orbitals represented by the red and blue ovals. The arrows 1, 2, and 3 indicate the bond directions in Eq. (1). (b) Schematic picture of the indirect paths for neighboring octahedra. θ denotes the deviation of the cation-ion-cation angle from 90°, which is caused by a trigonal distortion of the octahedra. The overlapping faint square represents an undistorted case with $\theta = 0°$. (c) θ dependence of the nearest-neighbor transfer t_1 in units of $(pd\pi)^2/\Delta_{dp}$; see Eq. (2) and the text. Schematic images of distorted octahedra are shown in the inset.

rotational operation in the e_g manifold. We will discuss the validity of this model by *ab initio* calculations later. We note that the t_1-t_3 model is particle-hole symmetric.

An interesting aspect in this model is that the transfer integrals are sensitively modulated by distortions of the octahedra. Let us demonstrate this by considering t_1 for a trigonal distortion by the compression or expansion of the octahedra perpendicular to the honeycomb plane as shown in Fig. 1(b). The modulation of the d-p-d transfer integral is approximately given as

$$t_1 = \frac{-4(pd\pi)^2 + [-2(pd\pi) + \sqrt{3}(pd\sigma)\cos^2\theta]^2}{2\Delta_{dp}} \sin\theta, \tag{2}$$

where $(pd\pi)$ and $(pd\sigma)$ are the Slater-Koster parameters [27] and Δ_{dp} (> 0) is the energy level splitting between the d orbitals of the TM cations and the p orbitals of the ligands. This relation shows that not only the magnitude but also the sign of t_1 is changed by θ. Assuming $(pd\sigma) = -2.2(pd\pi)$ [28], we plot t_1 as a function of θ in Fig. 1(c). Note that t_1 vanishes in the ideal octahedral case with $\theta = 0$. Considering this aspect, we investigate the electronic structure by taking t_1 and t_3 as free parameters in the following analysis.

Figure 2(a) displays the phase diagram for model (1). We find 12 states distinguished by the number, position, and form of band crossings at half filling (two electrons per site on average). The representative band structures in each state are shown in the Supplemental Material [29,33]. The band crossings evolve systematically while changing t_1 and t_3. For instance, from state No. 1 to No. 3, peculiar band crossings appear on the Γ-K lines at $t_3/t_1 \simeq 0.408$ in addition to the two DPNs at the K points (K and K'), and they split into two DPNs each by increasing t_3. The peculiar band crossing at state No. 2 is quadratic along the Γ-K lines but linear along the perpendicular directions; we call this type the semi-Dirac point node (sDPN) following previous works [34,35]. On the other hand, from state No. 3 to No. 7, four DPNs at and around the K point merge into a QBC, which is described by the standard effective Hamiltonian [29], and they split again into four; two of them merge again into an sDPN at the M point and finally disappear (gapped out). Similar changes are seen from state No. 10 to No. 12. In state No. 8 at $t_1/t_3 = 0.5$, the six DPNs on the Γ-K lines are interconnected to form a line node enclosing the Γ point. Meanwhile, in state No. 9 at $t_1/t_3 = -1$, the four DPNs merge with the DPN at the K point, and at the same time, the upper and lower bands meet at the Γ point to form a new DPN; the eigenstate of each DPN at the Γ or K point is eightfold degenerate, (spin 2)×(orbital 2)×(sublattice 2). We note that the six DPNs in state No. 7 originate in the "band folding" by the dominant t_3; suppose $t_1 = 0$, as the lattice sites connected by t_3 form a honeycomb structure with the twice larger lattice constant, the DPNs at the K points are copied to the midpoints of Γ-K lines, as discussed in a previous study [17].

The peculiar band crossings that we found can host topologically nontrivial states in the presence of the SOC. Although the orbital angular momentum is quenched in the e_g manifold, the e_g manifold is influenced by the SOC through the e_g-t_{2g} mixing in distorted octahedra. In particular, under a trigonal distortion, the leading contribution is given as [12]

$$H_{\mathrm{SOC}} = -\frac{\tilde{\lambda}}{2} \sum_i \sum_{mn} \sum_{\sigma\sigma'} c^{\dagger}_{im\sigma} (\hat{\tau}_y)_{mn} (\hat{\sigma}_z)_{\sigma\sigma'} c_{in\sigma'}, \tag{3}$$

where $\hat{\tau}_y$ $(\hat{\sigma}_z)$ is the Pauli matrix in orbital (spin) space; here, the xyz axes are taken as shown in the inset of Fig. 1(a) and the quantization axis of spin is taken along the [111] direction. The coupling constant is given as $\tilde{\lambda} = \lambda^2 \Delta_{\mathrm{tri}}/\Delta_{\mathrm{cub}}^2$, where λ is the atomic SOC for the d orbitals, Δ_{tri} is the trigonal field splitting of the t_{2g} orbitals, and Δ_{cub} is the e_g-t_{2g} splitting under the cubic crystal field.

In the presence of the effective SOC in Eq. (3), the electronic bands are split into four (twofold degenerate each). The band splitting is shown by plotting the minimum direct gap between the adjacent bands in Fig. 2(b); Δ denotes the value for the second- and third-lowest bands, while Δ' for the first and second (common to the third and fourth because the energy bands are symmetric with respect to zero energy). We also calculate the spin Chern number C_n for the nth-lowest band to characterize the topological nature of each gapped state [36]. Note that C_n is well defined as the effective SOC does not mix the different spin bands in the present case.

As shown in Figs. 2(b)–2(d), we find ten gapped states I–X with distinct spin Chern numbers in the presence of the effective SOC in Eq. (3). Between the gapped states, a band crossing occurs (i.e., Δ or Δ' vanishes), and the spin Chern numbers for the crossed bands change their values. Around $t_1/t_3 = 0.5$ and $t_1/t_3 = -1$, where the system realizes states No. 8 and No. 9 in the absence of the SOC, respectively, Δ and Δ' change in a complicated manner, as shown in the enlarged figures in Figs. 2(c) and 2(d). Our results indicate that the model (1) exhibits various types of topological transitions in the presence of the SOC.

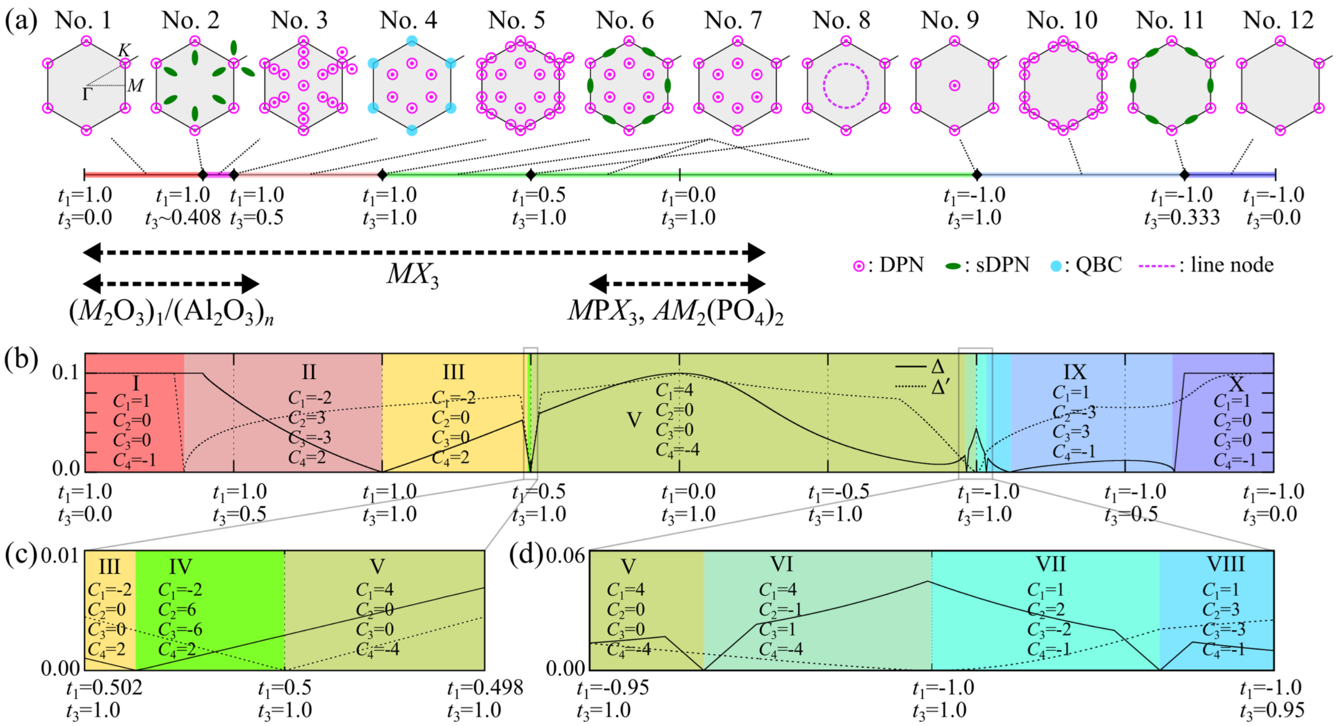

FIG. 2. (a) Phase diagram of the e_g-orbital tight-binding model without SOC at half filling. There are 12 states categorized by the number, position, and form of band crossings, which are schematically depicted in momentum space (the gray hexagons represent the first Brillouin zone). The results remain the same by changing the signs of t_1 and t_3 simultaneously. Candidate materials are also listed (see the main text). (b) The minimum direct gap opened by the effective SOC $\tilde{\lambda} = 0.1$ in Eq. (3); Δ (solid curve) is the value between the second- and third-lowest-energy bands, while Δ′ (dotted curve) between the first and second (common to the third and fourth). We also represent the values of the spin Chern number C_n for the nth-lowest band, which distinguish ten states labeled by I–X. (c) and (d) show the magnified pictures of (b) near the region with $t_1 = 0.5$ and $t_3 = 1.0$ and the region with $t_1 = -1.0$ and $t_3 = 1.0$, respectively.

Interestingly, the spin Chern numbers take unusually high magnitudes in some phases. This is conspicuous in the regions where t_3 is dominant, e.g., $C = \pm 6$ in state IV and $C = \pm 4$ in states V and VI. The high spin Chern numbers can be traced back to the increased number of band crossing points due to the band folding by t_3 in the absence of the SOC [Fig. 2(a)]; the folded bands contribute to enhance the Berry curvatures [17]. Such a folding effect is seen, for instance, in C_1 and C_4 in state V that are four times larger than those in states I and X; this is exactly shown at $t_1 = 0$ where the folded band perfectly overlaps with the original one. Thus, our results indicate that the honeycomb materials with a substantial contribution from t_3 potentially realize high topological numbers. The high topological number leads to the corresponding number of edge modes, whose multivalent nature would be useful for a practical application.

We also note that some bands have odd spin Chern numbers. An odd spin Chern number signals a nontrivial state such as the $\mathbb{Z}_2$ topological insulator protected by time-reversal symmetry [2]. Therefore, states I, VII, and X, where C_1 and C_4 are odd, share topological features with the $\mathbb{Z}_2$ topological insulators found in previous studies for [111] layers of the perovskite structure [12]. In addition, our results show that C_2 and C_3 in states II and VI and all C_n in states VI, VIII, and IX are also $\mathbb{Z}_2$ nontrivial.

Let us compare our tight-binding analysis with the previous *ab initio* studies for the honeycomb-layered TM compounds. Since our analysis so far is limited to a paramagnetic state, it would apply to weakly correlated materials such as 4d and 5d electron TM compounds. For instance, for the trichalcogenides MPX_3 (M = Pd, Pt, and X = S, Se), multiple DPNs, similar to those in state No. 7, were found around the Fermi level in the paramagnetic state for both 4d Pd and 5d Pt cases, while the former is a metastable state [17]. We note that $PdPS_3$ was synthesized in a bulk form about half a century before, while the electronic state was not studied [37]. Although for 3d-electron systems electron correlations may play a crucial role, a similar band structure was also seen for the e_g manifold in $BaFe_2(PO_4)_2$ though the Fermi level is in the t_{2g} manifold [24–26]. We note that our analysis also applies to the strongly correlated cases where the electron interaction stabilizes a largely polarized ferromagnetic state and the exchange potential splits the electronic bands into majority- and minority-spin manifolds. Indeed, for the trihalide $NiCl_3$ [19] and the layered corundum structure $(M_2O_3)_1/(Al_2O_3)_5$ [23], DPNs similar to those in state No. 1 appear in the spin-polarized e_g manifold. These observations are summarized below the phase diagram in Fig. 2(a) (for trihalides MX_3, see also below). Thus, our tight-binding analysis provides a systematic understanding of the existing *ab initio* results, and, furthermore, a useful guide for further material exploration.

To further confirm our scenario, we discuss the electronic structures of monolayer trihalides, with a focus on the 5d example AuX_3 (X = F, Cl, Br, and I), based on the *ab initio*

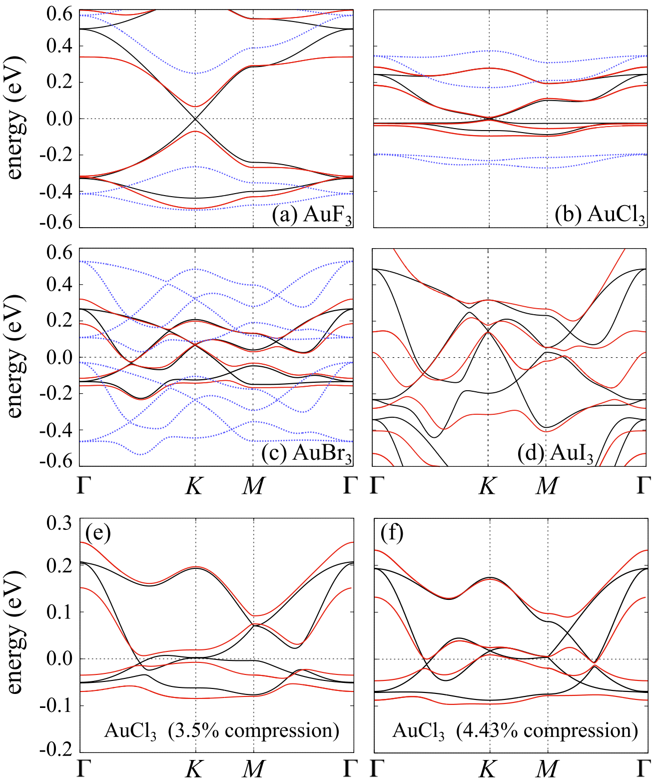

FIG. 3. Electronic band structures of monolayers of (a) $\mathrm{AuF_3}$, (b) $\mathrm{AuCl_3}$, (c) $\mathrm{AuBr_3}$, and (d) $\mathrm{AuI_3}$. The black (red) solid lines denote the nonrelativistic (relativistic) band structures in the paramagnetic state, which is stable for $\mathrm{AuI_3}$ and metastable for others. The blue dotted lines represent the nonrelativistic band structures of the stable magnetic states: the Nèel antiferromagnetic states for $\mathrm{AuF_3}$ and $\mathrm{AuCl_3}$ and the ferromagnetic state for $\mathrm{AuBr_3}$. The Fermi level is set to zero. (e) and (f) present the paramagnetic band structures for $\mathrm{AuCl_3}$ with 3.5% and 4.43% compression, respectively.

calculations by OPENMX code [38] (see Supplemental Material for the computational details [29]). Although previous experiments for AuX_3 reported other crystalline structures in the bulk form [39–41], we here consider the honeycomb monolayer form, which is obtained as a locally stable solution by structural optimization in our *ab initio* calculations. In the nonrelativistic calculations, we find that $\mathrm{AuI_3}$ is paramagnetic but others are magnetic: the Nèel antiferromagnetic states for $\mathrm{AuF_3}$ and $\mathrm{AuCl_3}$ and the ferromagnetic state for $\mathrm{AuBr_3}$ [blue dotted lines in Figs. 3(a)–3(c)] [29]. We show the band structures including the paramagnetic solutions (black solid lines) in Figs. 3(a)–3(d). Let us discuss the paramagnetic band structures in comparison with our tight-binding results. We find that $\mathrm{AuF_3}$ and $\mathrm{AuCl_3}$ possess DPNs at the K point, similar to state No. 1, while $\mathrm{AuBr_3}$ and $\mathrm{AuI_3}$ possess multiple DPNs on the Γ-K lines, similar to state No. 7 [see Fig. 2(a)]. Furthermore, as shown in Figs. 3(e) and 3(f), we find QBCs and sDPNs in $\mathrm{AuCl_3}$ with a few percent compression of the lattice structures, which are similar to states No. 4 and No. 6, respectively [29]. Table I summarizes the angle θ and the transfer integrals estimated by the maximally localized Wannier functions (MLWFs) [42,43] for these cases. These results are explained by our tight-binding analysis: The DPNs in $\mathrm{AuF_3}$ and $\mathrm{AuCl_3}$ are realized by the dominant nearest-neighbor transfer t_1 under a substantial compression of the octahedra (large θ), while those in $\mathrm{AuBr_3}$ and $\mathrm{AuI_3}$ result from the dominant third-neighbor transfer t_3 in almost ideal octahedra (small θ); the compressed $\mathrm{AuCl_3}$ locates in between. We confirm that the other transfers, e.g., second- and fourth-neighbor transfers, are less relevant compared to t_1 and t_3 [29], which supports our t_1-t_3 model. The results demonstrate the possibility of various band crossings in Fig. 2(a), through the chemical substitution and lattice distortions, once the paramagnetic state is stabilized. We note that the band crossings are retained even for the stable ferromagnetic solution for $\mathrm{AuBr_3}$ in each exchange-split band, as shown in Fig. 3(c). When the SOC is included in the relativistic calculations (red dotted lines in Fig. 3), all the DPNs are gapped out, as predicted in our tight-binding analysis. We note that the effect of the SOC is relatively large on $\mathrm{AuF_3}$ and $\mathrm{AuI_3}$, which is also understood by our tight-binding analysis with large Δ_{tri} and small Δ_{cub} in Eq. (3), respectively.

To summarize, we have theoretically investigated the electronic structure of the honeycomb-layered TM compounds with e_g electrons. We found that the e_g electronic dispersions show a series of peculiar band crossings, and in the presence of the SOC, they turn to be different topological states distinguished by the spin Chern numbers. These band crossings and topological states can be realized and controlled by chemical substitutions and distortions of octahedra. Indeed, we showed that the previous *ab initio* results are understood in a comprehensive manner according to our analysis. Furthermore, we proposed by *ab initio* calculations that trihalides MX_3 are

TABLE I. The angle θ [see Fig. 1(b)] and the transfer integrals between MLWFs obtained by the nonrelativistic *ab initio* calculations for AuX_3 (X = F, Cl, Br, and I) with the optimized structures and for $\mathrm{AuCl_3}$ with the compressed structures in the paramagnetic solution. Each value of the transfer integrals means $\langle d_m, \mathbf{0}|\, H\, |d_n, \boldsymbol{r}\rangle$, where H is the Hamiltonian of the system and $|d_m, \boldsymbol{r}\rangle$ is the d_m-like MLWF at site $\boldsymbol{r}$ ($m = 3z^2 - r^2$ or $x^2 - y^2$). We take $\boldsymbol{r} = \boldsymbol{R}_1$ and $\boldsymbol{R}_3$ in the left and right column, respectively [$\mathbf{0}$, $\boldsymbol{R}_1$, and $\boldsymbol{R}_3$ are illustrated in Fig. 1(a)]. The unit of transfer integrals is in meV.

	$\mathrm{AuF_3}$		$\mathrm{AuCl_3}$ (opt.)		$\mathrm{AuCl_3}$ (3.5%)		$\mathrm{AuCl_3}$ (4.43%)		$\mathrm{AuBr_3}$		$\mathrm{AuI_3}$	
θ	17.5°		9.1°		5.1°		3.4°		−0.4°		−3.2°	
$d_{3z^2-r^2}, d_{3z^2-r^2}$	−50	5	−16	0	−2	−3	1	−8	15	−22	53	−35
$d_{3z^2-r^2}, d_{x^2-y^2}$	0	0	0	0	0	0	0	0	0	0	0	0
$d_{x^2-y^2}, d_{3z^2-r^2}$	0	0	0	0	0	0	0	0	0	0	0	0
$d_{x^2-y^2}, d_{x^2-y^2}$	313	10	85	17	53	32	39	48	21	96	41	163

good candidates that realize a wide variety of the band topology. Our findings would stimulate further material exploration toward the exotic phases of matter in the honeycomb-layered materials. They would also offer a interesting platform for the study of electron correlation effects on various topological states.

Y.S. thanks E.-G. Moon for useful comments. The authors acknowledge T. Miyake for helpful comments on the *ab initio* calculations. Y.S. is supported by the Japan Society for the Promotion of Science through a research fellowship for young scientists and the Program for Leading Graduate Schools (MERIT).

[1] K. S. Novoselov, A. K. Geim, S. V. Morozov, D. Jiang, Y. Zhang, S. V. Dubonos, I. V. Grigorieva, and A. A. Firsov, Science **306**, 666 (2004).

[2] C. L. Kane and E. J. Mele, Phys. Rev. Lett. **95**, 146802 (2005).

[3] C. L. Kane and E. J. Mele, Phys. Rev. Lett. **95**, 226801 (2005).

[4] Y. Yao, F. Ye, X.-L. Qi, S.-C. Zhang, and Z. Fang, Phys. Rev. B **75**, 041401 (2007).

[5] C.-C. Liu, W. Feng, and Y. Yao, Phys. Rev. Lett. **107**, 076802 (2011).

[6] K. Sun, H. Yao, E. Fradkin, and S. A. Kivelson, Phys. Rev. Lett. **103**, 046811 (2009).

[7] J. M. Murray and O. Vafek, Phys. Rev. B **89**, 201110 (2014).

[8] O. Vafek and K. Yang, Phys. Rev. B **81**, 041401 (2010).

[9] F. Zhang, H. Min, M. Polini, and A. H. MacDonald, Phys. Rev. B **81**, 041402 (2010).

[10] R. Nandkishore and L. Levitov, Phys. Rev. Lett. **104**, 156803 (2010).

[11] S. Pujari, T. C. Lang, G. Murthy, and R. K. Kaul, Phys. Rev. Lett. **117**, 086404 (2016).

[12] D. Xiao, W. Zhu, Y. Ran, N. Nagaosa, and S. Okamoto, Nat. Commun. **2**, 596 (2011).

[13] A. Rüegg and G. A. Fiete, Phys. Rev. B **84**, 201103 (2011).

[14] K.-Y. Yang, W. Zhu, D. Xiao, S. Okamoto, Z. Wang, and Y. Ran, Phys. Rev. B **84**, 201104 (2011).

[15] A. Rüegg, C. Mitra, A. A. Demkov, and G. A. Fiete, Phys. Rev. B **85**, 245131 (2012).

[16] D. Doennig, S. Baidya, W. E. Pickett, and R. Pentcheva, Phys. Rev. B **93**, 165145 (2016).

[17] Y. Sugita, T. Miyake, and Y. Motome, Phys. Rev. B **97**, 035125 (2018).

[18] J. He, S. Ma, P. Lyu, and P. Nachtigall, J. Mater. Chem. C **4**, 2518 (2016).

[19] J. He, X. Li, P. Lyu, and P. Nachtigall, Nanoscale **9**, 2246 (2017).

[20] C. Huang, J. Zhou, H. Wu, K. Deng, P. Jena, and E. Kan, Phys. Rev. B **95**, 045113 (2017).

[21] X.-L. Sheng and B. K. Nikolić, Phys. Rev. B **95**, 201402 (2017).

[22] J. F. Afonso and V. Pardo, Phys. Rev. B **92**, 235102 (2015).

[23] O. Köksal, S. Baidya, and R. Pentcheva, Phys. Rev. B **97**, 035126 (2018).

[24] Y.-J. Song, K.-W. Lee, and W. E. Pickett, Phys. Rev. B **92**, 125109 (2015).

[25] Y.-J. Song, K.-H. Ahn, W. E. Pickett, and K.-W. Lee, Phys. Rev. B **94**, 125134 (2016).

[26] H.-S. Kim and H.-Y. Kee, npj Quantum Mater. **2**, 20 (2017).

[27] J. C. Slater and G. F. Koster, Phys. Rev. **94**, 1498 (1954).

[28] W. A. Harrison, *Electronic Structure and the Properties of Solids* (Dover, New York, 1989).

[29] See Supplemental Material at http://link.aps.org/supplemental/10.1103/PhysRevB.99.041101 for electronic band structures of the tight-binding model in Eq. (1), the effective Hamiltonian for QBCs, the computational details of *ab initio* calculations, the total energy comparison by *ab initio* calculations, and the detailed information on transfer integrals of candidate materials obtained by *ab initio* calculations, which includes Refs. [30–32].

[30] T. Ozaki, Phys. Rev. B **67**, 155108 (2003).

[31] T. Ozaki and H. Kino, Phys. Rev. B **69**, 195113 (2004).

[32] J. P. Perdew, K. Burke, and M. Ernzerhof, Phys. Rev. Lett. **77**, 3865 (1996).

[33] Note that peculiar band crossings, such as DPNs and QBCs, are also found apart from half filling.

[34] V. Pardo and W. E. Pickett, Phys. Rev. Lett. **102**, 166803 (2009).

[35] S. Banerjee, R. R. P. Singh, V. Pardo, and W. E. Pickett, Phys. Rev. Lett. **103**, 016402 (2009).

[36] T. Fukui, Y. Hatsugai, and H. Suzuki, J. Phys. Soc. Jpn. **74**, 1674 (2005).

[37] W. Klingen, R. Ott, and H. Hahn, Z. Anorg. Allg. Chem. **396**, 271 (1973).

[38] See http://www.openmx-square.org/.

[39] E. S. Clark, D. H. Templeton, and C. H. MacGillavry, Acta Crystallogr. **11**, 284 (1958).

[40] F. W. B. Einstein, P. R. Rao, J. Trotter, and N. Bartlett, J. Chem. Soc. **A**, 478 (1967).

[41] K. P. Lörcher and J. Strähle, Z. Naturforsch. B **30**, 662 (1975).

[42] N. Marzari and D. Vanderbilt, Phys. Rev. B **56**, 12847 (1997).

[43] I. Souza, N. Marzari, and D. Vanderbilt, Phys. Rev. B **65**, 035109 (2001).